View Article Online
DOI: 10.1039/D4CP03087G

Mechanistic Insights into CO_2 Activation on Pristine, Vacancy-containing and Doped Goldene: A Single-Atom Layer of Gold

Kamal Kumar[1], Nora de Leeuw[2], Jost Adam[3,4] and Abhishek Kumar Mishra[1]*

[1]Department of Physics, Applied Science Cluster, School of Advanced Engineering, UPES,
Dehradun, Uttarakhand 248007, India

[2]Department of Chemistry, University of Leeds, Leeds LS2 9JT, UK

[3]Computational Materials and Photonics, FB 16, University of Kassel, Wilhelmshöher Allee 71,
34121 Germany

[4]Center for Interdisciplinary Nanostructure Science and Technology, University of Kassel,
Heinrich-Plett-Straße 40, 34132 Kassel, Germany

ABSTRACT

Goldene, a one-atom-thick gold sheet, is an emerging graphene-like flat 2-dimensional material. In this study, the geometrical and electronic properties, as well as CO_2 adsorption characteristics, of the pristine, vacancy-containing, and X-doped (X=Al, B, S, P, and N) goldene sheets have been investigated by employing first-principles calculations based on the density functional theory. The distribution of energy levels and interaction between the CO_2 molecule and goldene (pristine, partially vacant, and doped) is discussed through the projected density of states (PDOS), electronic band structure (EBS), and Bader charge analysis. We found that CO_2 adsorbs physically on pristine goldene (PG) with an adsorption energy of -24.6 kJ/mol, while the creation of a mono-vacancy (MG), di-vacancy (DG) or tri-vacancy (TG) results in only marginal increases in the binding strength of CO_2 with the goldene, and the nature of the interaction remains physisorption. The calculated adsorption energies of CO_2 at a MG, DG and TG are -25.60, -25.10, and -30.90 kJ/mol respectively. Among a range of dopants considered in this work, doping by boron and nitrogen atoms causes goldene to absorb CO_2 chemically, with relatively large adsorption energies of -138.9 and -163.7 kJ/mol and Bader charge transfers of -1.22 e^- and 0.66 e^- respectively. Our findings provide an in-depth understanding of the electronic properties of pure, vacancy-containing, and doped goldene, which can aid their potential application in CO_2 activation and conversion.

Keywords: Goldene, CO_2 activation, vacancies, dopants, DFT

Corresponding author email: akmishra@ddn.upes.ac.in; mishra_lu@hotmail.com

View Article Online
DOI: 10.1039/D4CP03087G

1. Introduction

Goldene is a new member of the 2-dimensional family of materials, which was first predicted computationally by Yang *et al.* in 2015 as a robust and highly stable single-atom-thick freestanding hexagonal close-packed metallic 2D flat monolayer of gold (Au) atoms [1]. They computationally designed four different configurations (hexagonal close-packed, honeycomb, square, and tetrally coordinated) of 2D Au-nanosheets, but they found that the hexagonal close-packed atomic arrangement is the most stable configuration in 2D space [1]. Subsequently, in 2019, Wang *et al.* successfully synthesized this single-atom-thick freestanding Au membrane experimentally, using in situ de-alloying to a thickness of 0.6 nm framed in bulk crystal[2]. In 2022, Sharma *et al.* reported a technique to synthesize one-atom-thick freestanding gold crystals and a 2D periodic arrangement of Au atoms on a sapphire substrate using the thermal evaporation method and they named this nanosheet goldene. HRTEM and AFM imaging techniques confirmed its 1-2 Å thickness and herringbone-honeycomb crystal lattice[3]. In 2023, Kashiwaya *et al.* prepared goldene by wet chemical etching of Ti_3C_2 from Ti_3AuC_2, as a nano-laminated ceramic of the MAX phase obtained by substituting Au with Si in Ti_3SiC_2[4]. Molecular dynamics simulation-based theoretical studies suggest that Au surfaces can be promising adsorbent materials for CO_2 adsorption[5], whereas Au-based catalysts are now recognized to contribute to various chemical reactions, including in catalysis and selective oxidation[6]. Au nanoclusters have shown superior catalytic activity in CO oxidations[6] at low temperatures, whereas adsorption of H_2O, O_2, thiols, di-sulfide, and CO on the Au surface has been reported earlier in the literature[7–10].

Since the exfoliation of graphene, extensive research has been conducted on 2D nanostructures, resulting in the design and synthesis of various ultrathin nanomaterials [11,12]. Hexagonal boron nitride (h-BN), metal-organic frameworks (MOFs), transition metal dichalcogenides (TMDCs), and MXenes are some additional candidates within the 2D materials family that exhibit intriguing characteristics that sometimes outperform those of graphene[13,14]. These materials provide atomic-level engineering, allow the creation of defined pore shapes and sizes, easy functionalization, and reversible adsorption-desorption phenomena for optimal adsorption of gas molecules [15–17]. Generally, pristine nanosheets show weak physisorption towards molecules and nanoscale engineering of these materials therefore becomes crucial in the development of cost-effective adsorbent materials [18–20]. Some key engineering techniques employed in designing and developing adsorbent materials are defect engineering, doping, surface functionalization and strain

View Article Online
DOI: 10.1039/D4CP03087G

engineering[21,22]. Defects in these 2D materials can enhance their molecule adsorption capacity by generating additional adsorption sites, improving adsorption kinetics, and altering electronic properties[23,24]. The literature demonstrates various 2D materials whose adsorption capacity is enhanced through the introduction of defects[25,26]. The density functional theory (DFT) study of Wang *et al.* revealed that the CO_2 molecule adsorbs on pristine graphene with an adsorption energy of only -0.23 eV (-22.19 kJ/mol). Yet, upon creating a mono-atomic vacancy defect, the adsorption energy increased to -0.39 eV (-37.63 kJ/mol), shifting from weak to strong physisorption [25]. Hussain *et al.* studied the adsorption behavior of different gas molecules on pure and defective silicene[26]. Their study found that the CO_2 molecule adsorbs weakly onto silicene with an adsorption energy of just -0.09 eV (-8.68 kJ/mol), but when a mono-vacancy is created in the silicene nanosheet, the binding energy of CO_2 increases by 17 times to -1.64 eV (-158.24 kJ/mol)[48]. The presence of the mono-vacancy not only increased the adsorption energy of CO_2 on the silicene nanosheet, but also enhanced the adsorption energies of H_2S and SO_2 gas molecules from -0.19 eV (-18.3 kJ/mol) and -0.80 eV (-77.19 kJ/mol) to -0.98 eV (-94.56 kJ/mol) and -2.87 eV (-276.9 kJ/mol)), respectively, along with structural deformation of the molecules due to the strong Van der Waals interaction[26].

Another important method to tailor the activity and interaction between adsorbate molecules and the adsorbent material is the introduction of foreign atoms, i.e. by doping or substitution[27–29]. Doping can change the electronic behavior of materials by modifying the distribution of energy levels in the electronic band structure (EBS) by changing the electron density around the dopant atom, leading to an expansion in the material applications [30,31]. Depending on the type of doping (n-type or p-type) and nature of the dopant, numerous research articles are available on 2D materials for different purposes, including in energy storage, gas sensing and catalysis[32,33]. Boron (B) and aluminum (Al) are the two most widely explored p-type elements of group 13 of the Periodic Table in doping processes [34,35]. Rad *et al.* found that the weak physisorption of CO_2, H_2O and CO molecules on a pure graphene sheet could be significantly increased from the region of physisorption (-3.7, -5.8 and -1.6 kJ/mol, respectively) to the region of chemisorption (-102.6, -120.5 and -53.8 kJ/mol respectively) by doping with Al atoms[36]. The theoretical study of Monshi *et al.* suggests that the adsorption energy of the H_2S gas molecule can be increased from 0.58 eV (-55.96 kJ/mol) to -1.02 eV (-98.41 kJ/mol) through doping by Al atoms in intrinsic germanene, owing to a strong charge transfer of -0.373 e^- between the doped germanene and the H_2S

View Article Online
DOI: 10.1039/D4CP03087G

molecule[37]. Zheng *et al.* explored the adsorption behavior of CO_2 molecules on intrinsic and doped graphene, and their investigation revealed that B-doped graphene can be a promising adsorbent material for CO_2 capture with an adsorption energy of -0.86 eV(-82.98 kJ/mol)[38]. For n-type doping, nitrogen (N) and phosphorous (P) have gained considerable attention[39,40]. Monshi *et al.* employed DFT calculations to investigate the gas sensing performance of pristine and doped germanene. Their study indicated weak adsorption of CO_2 and H_2S on pure germanene with adsorption energies of -0.42 eV (-40.52 kJ/mol) and -0.58 eV (-55.96 kJ/mol), whereas doping by N and B atoms enhanced the interaction between these molecules and the germanene sheet to -0.96 eV(-92.63 kJ/mol) and -0.50 eV (-48.24 kJ/mol) for CO_2 and -0.66 eV (-63.68 kJ/mol) and -0.61 eV (-58.86 kJ/mol) for the H_2S molecule [37]. Doping of B and Al atoms in graphene has been found to increase the sensitivity of graphene sheets towards the detection of toxic gases (NO_2 and NO) by enhancing the interaction of graphene with gas molecules[31]. N- and P-doped graphene has been proposed as a promising candidate for different energy conversion reactions, including CO_2 reduction reactions (CO_2RR) and oxygen reduction reactions (ORR)[41,42]. Seema et al. have studied the gas adsorption capacity (for N_2, CO_2, H_2 and CH_4) of S-doped microporous carbon materials[44], which revealed that these S-doped materials exhibit a large adsorption capacity (4.5 mmol g^{-1}) and high selectivity for CO_2 molecules over H_2, N_2, and CH_4[43]. Doping with B and N atoms has been found to increase the strength of interaction between CO_2 and graphene-like BCN materials[44,45]. In addition, some hydrophobic surfaces have also been found suitable for CO_2 capture[46].

Here, we report our investigation of the adsorption and activation of CO_2 on pristine (PG), vacancy-containing (VG), and X-doped (X=B, Al, N, P, S) goldene sheets. We have explored the formation of mono-, di-, and tri-vacancies, denoted by MG, DG, and TG, respectively. The adsorbent characteristics are characterized through adsorption energy calculations, partial density of states (PDOS) analysis, changes in the electronic band structure (EBS), and charge density plots. The results of our investigation will provide insight into surface-adsorbate interaction phenomena, which improve the reactivity of goldene-based substrates.

2. Computational Methodology

The calculations in this work are based on the density functional theory (DFT) as implemented in the *Quantum Espresso* simulation package [47]. Our calculations employ the generalized gradient

View Article Online
DOI: 10.1039/D4CP03087G

approximation (GGA)[48] as proposed by Perdew, Burke and Ernzerhof (PBE),[49] to describe the electronic structure of the considered systems[50]. For an accurate representation of the dispersion interactions, Van der Waals (vdW) interactions were implemented via the Grimme-D3 method[51]. The projector-augmented wave (PAW) method was used for the precise modelling of both valence (outer) and core (inner) electrons[52]. A well-converged energy cutoff of 42 Ry along with a 9×9×1 k-points mesh to sample the Brillouin zone were utilized in the geometry optimization and post-relaxation calculations. The atomic positions were relaxed until all forces came to within 0.01 eV on each atom and the total energy change was minimal (within 10^{-7}). To eliminate the interactions between neighbouring slabs, a vacuum of 12 Å was introduced in the Z direction, i.e. perpendicular to the monolayer. A 5×5×1 supercell, consisting of 25 Au atoms, was considered when studying the CO_2 activation calculations. The vacancy defect formation energy (E_f), binding energy (E_{X_b}) of different dopants (X= Al, B, N, P, and S), and adsorption energy of CO_2 on various goldene sheets are determined by equations (1), (2) and (3) respectively.

$$\mathrm{E_f} = \mathrm{E_{defect}} - \frac{(N-n)}{N} E_{\mathrm{sheet}} \tag{1}$$

$$\mathrm{E_{X\_b}} = \mathrm{E_{Au+X}} - (\mathrm{E_{sheet}} + \mathrm{E_X}) \tag{2}$$

$$\mathrm{E_{ad}} = \mathrm{E_{sheet+CO2}} - (\mathrm{E_{sheet}} + \mathrm{E_{CO2}}) \tag{3}$$

Where in equation 1, N represents the total number of Au toms in the goldene sheet and n denotes number of Au atoms removed from the goldene sheet. E_{defect} is the energy of the goldene sheet with vacancy defect(s).

E_{Au+X}, $E_{sheet+CO2}$, E_{sheet}, E_{CO2} and E_X are the total energies of X-doped goldene, goldene with adsorbed CO_2, pristine goldene, the CO_2 molecule, and a single X atom, respectively.

3. Results and Discussion

In this section, we present our results on the structural details of pristine goldene, followed by the results and discussion on the effects of vacancies (mono, di, and tri) and doping (B, Al, N, P and S) on the electronic and geometrical properties of the goldene sheets. Subsequently, we discuss the CO_2 adsorption results on the pristine, vacancy-containing, and doped goldene sheets.

3.1 Structural Details and Electronic Properties of Pristine Goldene (PG)

View Article Online
DOI: 10.1039/D4CP03087G

The 2D goldene monolayer is a hexagonal closed-packed (HCP) nanosheet of Au atoms that belongs to the P6/mmm space group (#191)[1]. The unit cell of goldene consists of only one Au atom, shown in **Figure 1(a)** [58,61]. The cell parameter of goldene is 2.75 Å, which is smaller than that of silicene (3.86 Å)[53] but larger than that of graphene (2.46 Å)[54]. Unlike silicene, germanene, and plumbene, the goldene monolayer is a flat 2D nanosheet similar to graphene. Our calculated cell parameter, Au-Au bond length, and bond angle of PG are 2.74 Å, 2.73 Å, and 60.0°, respectively, which are in good agreement with earlier reported experimental[1] and computational[4] works (**Table 1**). To gain a deeper understanding of the electronic properties of goldene, projected density of states (PDOS) and electronic band structure (EBS) have been computed and are plotted in **Figure 1b**, which shows a finite number of electronic states around the Fermi level, indicating its metallic character. A similar distribution of electronic energy levels was reported earlier by Yang *et al.* [1]. The electron of the outermost s-orbital of the Au atom ($6s^1$) is attached to the core with a weak electrostatic interaction. It can move freely throughout the material, i.e. in the conduction band (above the Fermi level) at room temperature. This phenomenon can be seen easily from the EBS, where one of the energy levels of the valence band crosses the Fermi level between two high symmetry K-points Γ and K. Thus, the d-electrons which occupy the outer shell of the Au atom and are involved in chemical bonding, jump into an energy state where they behave like free electrons. PDOS analysis shows that for a PG nanosheet, the significant contribution to the valence band arises from the d-orbitals of the Au atom.

Table 1 Calculated values of the lattice cell parameters a and b (Å), bond angle θ (°), and bond length l (Å) of pristine goldene (PG) and comparison with earlier experimental[4] and computational[1] works

	a	**b**	**θ**	**l**
Present Work	2.74	2.74	60°	2.73
Yang *et al.*[1]	2.75	2.75	---	2.75
Kashiwaya *et al.*[4]	2.75	2.75	---	2.62

View Article Online
DOI: 10.1039/D4CP03087G

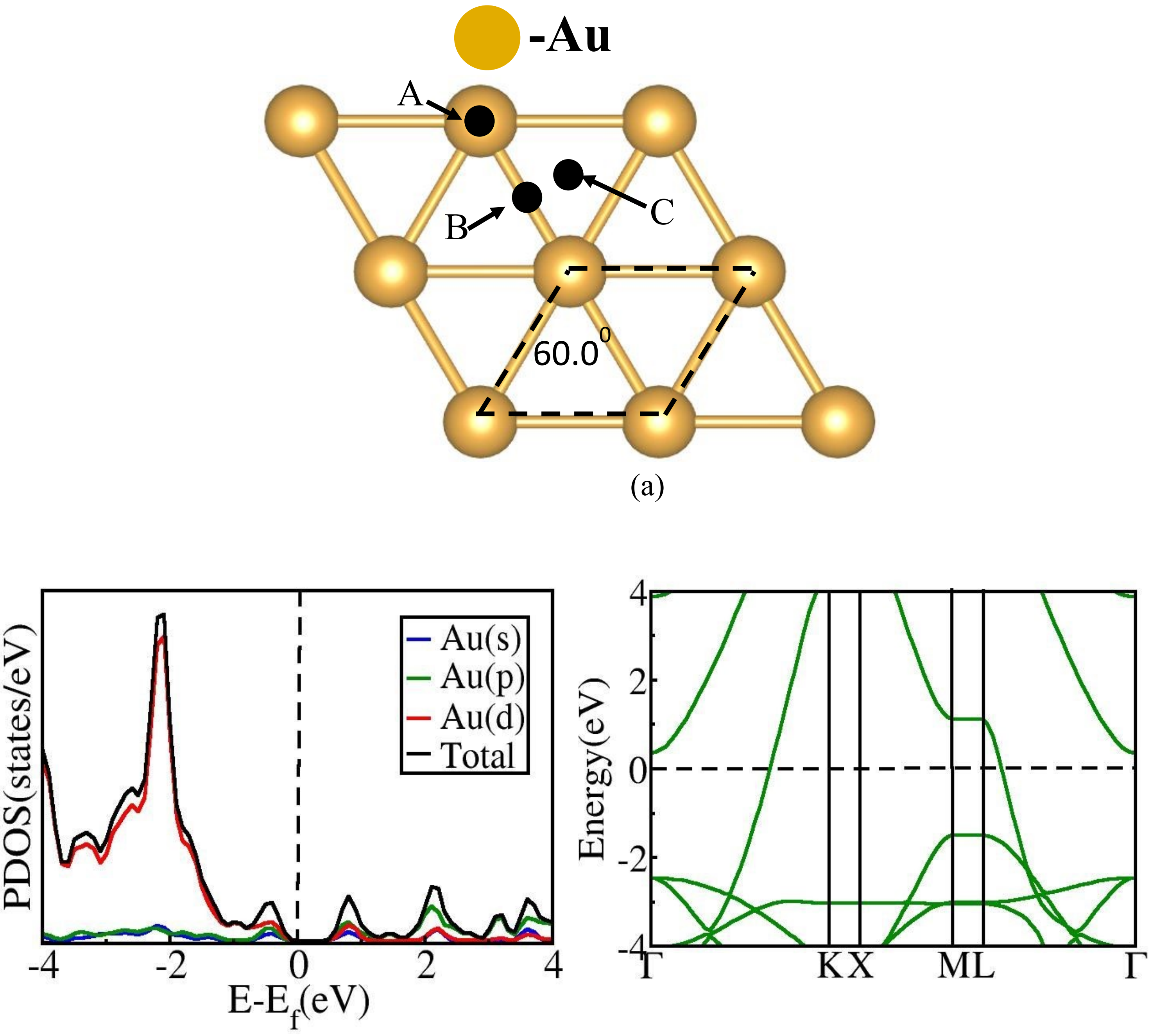

(a)

(b)

Figure 1 (a) Relaxed supercell of pristine goldene (PG) with highlighted unit cell consisting of one Au atom (b) Projected density of states (PDOS) (left) and electronic band structure (EBS) of pristine goldene sheet (right), where dotted black lines in these plots represent the Fermi level (E_f =0). We have marked the investigated CO_2 adsorption sites on goldene as A, B, and C in Figure

View Article Online
DOI: 10.1039/D4CP03087G

1a. The unit cell of goldene consists of only one Au atom (Figure 1a) and PDOS as well as EBS plots (Figure 1b shows the metallic character of goldene)

3.2 Vacancies in Goldene

In this section, we investigate the formation of mono-, di-, and tri-atom vacancies in the goldene sheet, where we have first considered the effect of supercell size, i.e. how the vacancy concentration affects the defect formation energies. We first calculated the defect formation energy (E_f) for a mono vacancy from equation (1) to be -1.59, -1.56, and -1.54 eVs for a 4×4×1 (6.25 % coverage), 5×5×1 (4.00 % coverage) and 6×6×1 (2.78 % coverage) supercell, respectively [Figure 2 (a)]. In the case of di-vacancies [Figure 2 (b)], the defect formation energies for 4×4×1 (12.5 %), 5×5×1 (8.00 %), and 6×6×1 (5.56 %) supercells were calculated to be -3.00 eV, -2.93 eV and -2.80 eV, respectively. For the formation of tri-vacancies, we have considered three different configurations, namely an angle, line and triangle, as shown in **Figure 2(c)**. The E_f values for the triangle, line, and angle defects were calculated at -3.65 eV, -4.16 eV and -4.25 eV, respectively (in a 5×5×1 supercell with a 12.00% defect concentration), indicating that the angle-type is the most stable tri-vacancy in the goldene sheets. The magnitude of these E_f energies are greater than in silicene with mono- (-3.62 eV), di- (-4.32 eV), and tri-vacancies (-5.79 eV)[48], indicating the larger requirement of energy to form vacancies in goldene compared to silicene with goldene therefore being more resistant against the formation of vacancies in its structure. In all three cases, i.e. mono-, di-, and tri-vacancy structures, Au-Au bond lengths near the vacancies contract from 2.74 Å to 2.68 Å, while the bond angle increases up to 61.15° from its initial value of 60°. This change in bond lengths and bond angles of surrounding atoms is a common consequence of defect formation due to the redistribution of interatomic forces to achieve lower energy states. Creating mono-, di-, and tri-vacancies yields six, eight, and nine dangling bonds, respectively. Table 2 summarizes the calculated E_f along with structural parameters of various vacancy-containing systems of the goldene monolayer. The relaxed structures of MG, DG and TG for the 5×5×1 supercells are shown in Figure 2, while the structures of the 4×4×1 and 6×6×1 supercells are shown in Figure S1 of the supplementary information (SI). We have plotted the PDOS (and EBS) of mono, di-and angle tri-vacancy (angle) goldene sheets in **Figure 3** (and **Figure S2)**, where we note zero band gap in all three cases. We observed that the goldene sheet preserves its metallic nature and flat geometrical structure without buckling even after vacancy formation.

View Article Online
DOI: 10.1039/D4CP03087G

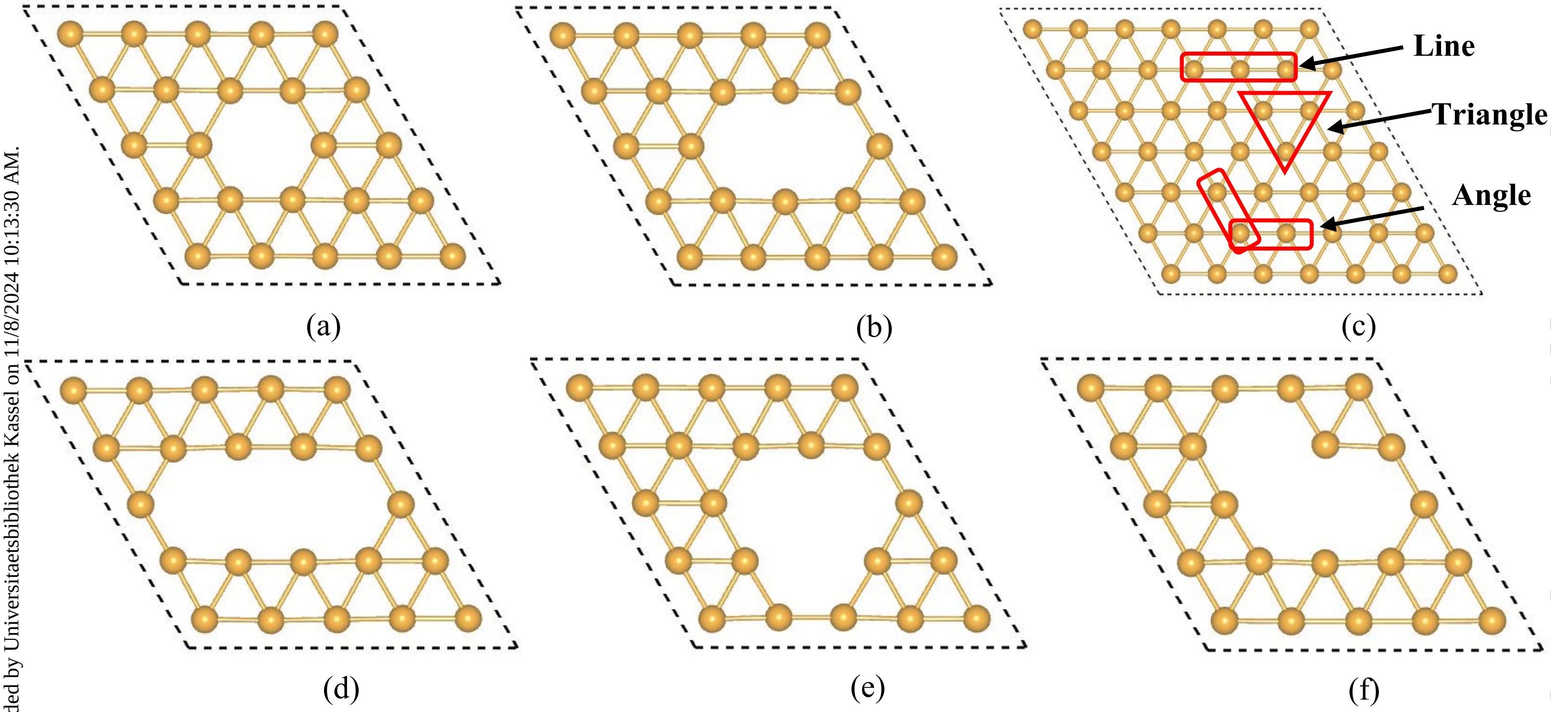

Figure 2. Relaxed structures of (a) mono-vacancy goldene (MG) and (b) di-vacancy goldene (DG) sheets, (c) three possible cases of a tri-vacancy in goldene (TG) sheet, with relaxed structures of (d) line tri-vacancy, (e) triangle tri-vacancy, and (f) angle tri-vacancy.

Table 2 Defect formation energy E_f (eV), Au-Au bond length l (Å), Au-Au bond angle θ (°) of MG, DG and TG systems

System	Supercell/Defect Concentration	E_f	l	θ
MG	4×4×1 (6.25%)	-1.59	2.69	58.32°
	5×5×1 (4.00%)	-1.56	2.76	61.15°
	6×6×1 (2.78%)	-1.54	2.74	60.12°
DG	4×4×1 (12.5%)	-3.00	2.70	59.99°
	5×5×1 (8.00%)	-2.93	2.80	61.32°
	6×6×1 (5.56%)	-2.80	2.70	58.44°
TG	4×4×1 (18.75%)	-3.68	2.71	60.11°
	5×5×1 (12.00%)	-3.65	2.76	61.01°
	6×6×1 (8.34%)	-3.62	2.75	60.84°

DOI: 10.1039/D4CP03087G

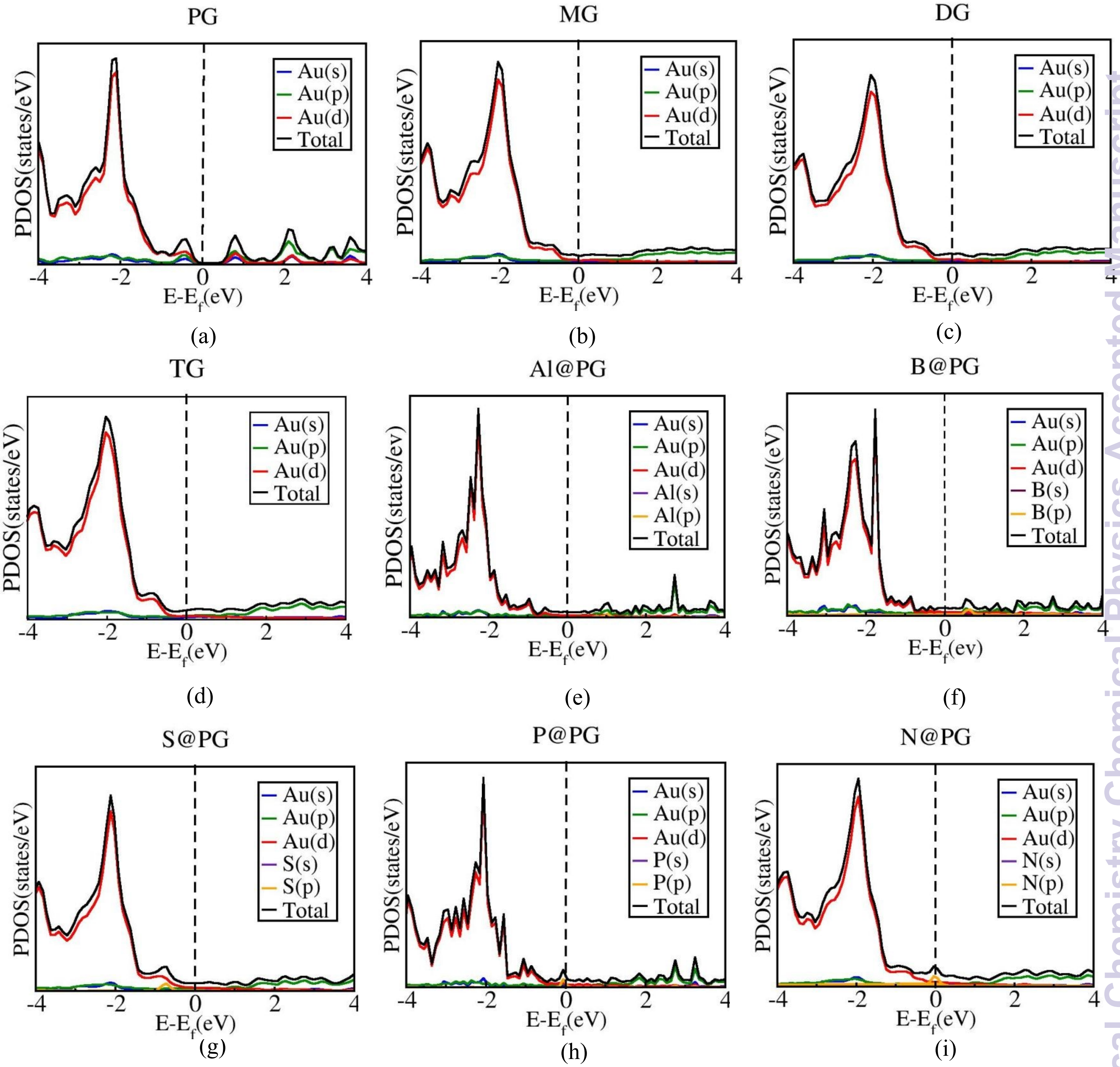

(a) (b) (c)

(d) (e) (f)

(g) (h) (i)

Figure 3 PDOS of (a)PG, (b) MG, (c) DG, (d) TG, (e) Al@PG (f) B@PG (g) S@PG (h) P@PG and (i) N@PG systems. The Fermi level (E_f) is set to zero and is represented by a dotted line. In

View Article Online
DOI: 10.1039/D4CP03087G

all considered systems, the major contribution in the PDOS comes from the d-orbital of the Au atoms.

3.3 X (=Al, B, S, N, P) doped goldene (X@PG)

The structural and electronic properties of doped goldene sheets are discussed in this section. In **Table 3**, we have given the structural parameters and binding energies (E_{X_b}) of doped X atoms in a goldene 2D sheet, as calculated using **equation (2).** The binding energies of Al, B, S, N, and P atoms with goldene are calculated to be -5.82, -4.65, -4.52, -3.88, and -5.23 eV, respectively. Goldene retains its flat structure even after doping with the various elements **[Figure 4]**. A quick comparison of the Al atom binding with similar 2D materials reveals that the magnitude of E_{Al_b} of Al@PG is higher than the binding energy of Al-doped silicene (-5.52eV)[55] and Al-doped germanene (-5.00 eV)[56] indicating that when the Al atom is doped into goldene, it makes stronger chemical bonds with the crystal lattice of goldene compared to its bonding with germanene and silicene 2D materials. The maximum elongation of 3.29% in the Au-Au bond length is obtained through B doping followed by N atom doping (2.56%), where the Au-Au bond length has increased to 2.82 and 2.80 Å, respectively, in B and N atoms doped goldene sheets, making these structures susceptible to any chemical/molecular activity. The variation in bond length between the Au atoms (near and away from X atoms) is due to the dopant atoms' sizes and self-charge characteristics.

Next, we investigated the PDOS of different doped goldene sheets and observed finite electronic states at the Fermi level, as shown in **Figure 3,** indicating their metallic character**.** EBSs of these doped goldene sheets are given in **Figure S2.** We have plotted the charge density difference for different doped structures in **Figure 5,** and a closer look at charge transfer ($\Delta \mathbf{q_X}$) in **Table 3** indicates that when PG is doped with Al and B atoms, they act as electron donors. In contrast, S, P and N atoms act as electron acceptors. N, the most electronegative element among the various dopants, accommodates the most charge of -0.52e. **Figure 3** shows the relaxed geometries of all X@PG systems in this work.

The strong binding of B or N to a 2D gold sheet is driven by significant charge transfer owing to differences in electronegativity, orbital hybridization between gold and the dopant atoms, and possible local structural changes that stabilize the system. B donates electrons to the goldene sheet, while N attracts electrons from it, both of which strengthen the bonding in their respective ways. The lack of significant charge transfer in Al-, S-, and P-doped goldene sheets is likely due to

View Article Online
DOI: 10.1039/D4CP03087G

similar electronegativity values to Au (S, P) or larger atomic size and poor orbital overlap (Al). The orbital interactions and hybridization for these elements do not facilitate significant charge transfer, unlike when doping with B or N, which both have greater electronegativity differences and better orbital compatibility with Au.

Table 3 Binding energy E_{X_b} (eV), bond lengths l (Å), Au-Au bond angle θ (°), and charge transfer Δq_X of X@PG systems

Dopant (X)	**E_{X_b}**	**l**		**θ**		**Δq_X**
		Au-Au	**Au-X**	**Au-Au**	**Au-X**	
Al	-5.82	2.76	2.68	61.99°	60.00°	2.93
B	-4.65	2.82	2.64	61.70°	60.00°	0.18
S	-4.52	2.76	2.72	61.46°	60.00°	-0.38
P	-5.23	2.78	2.69	60.88°	60.00°	-0.04
N	-3.88	2.80	2.66	61.24°	60.00°	-0.52

View Article Online
DOI: 10.1039/D4CP03087G

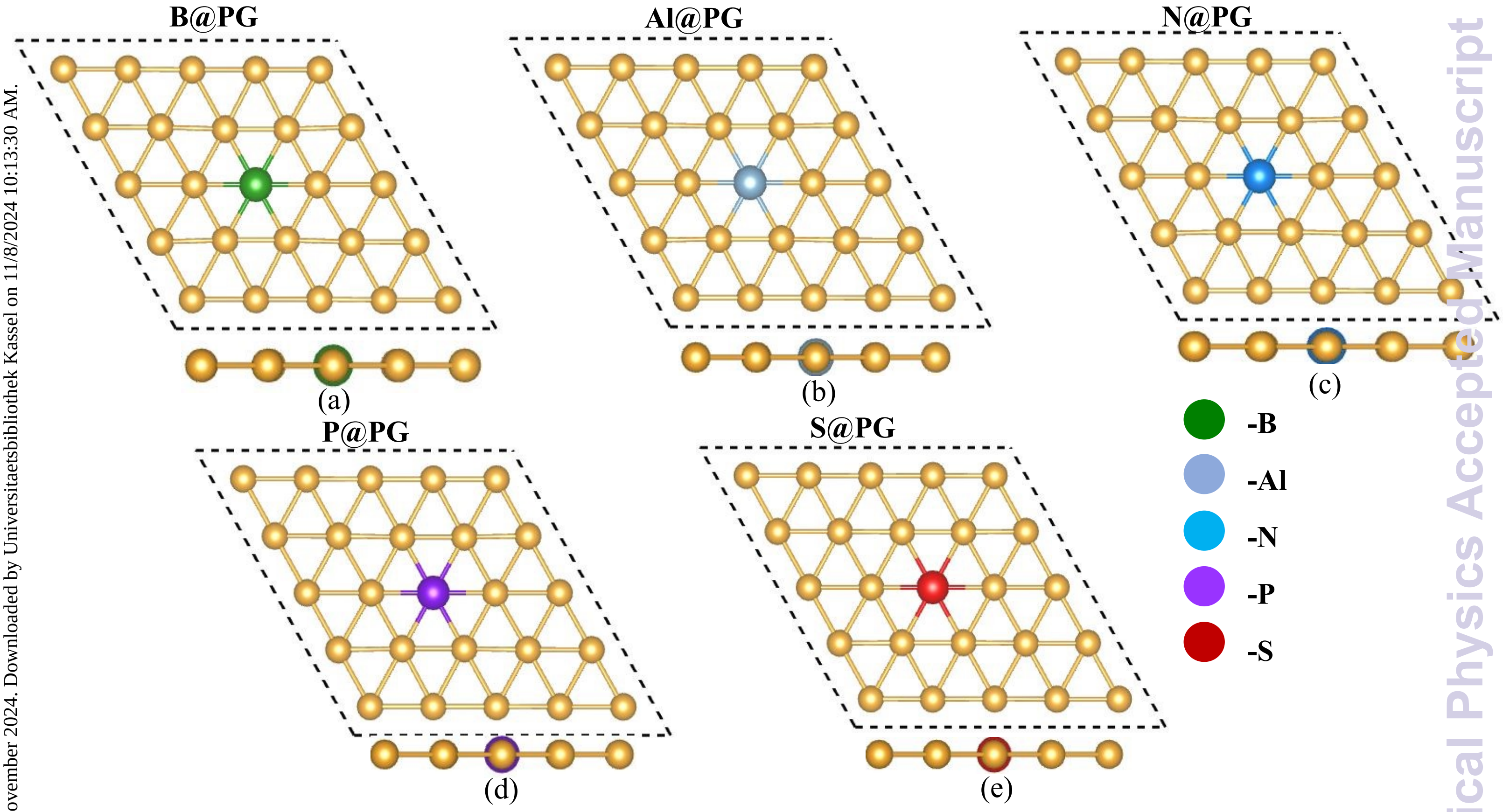

Figure 4 Top and side views of relaxed (a) B@PG, (b) Al@PG, (c) N@PG, (d) P@PG, and (e) S@PG for 5×5×1 supercells of goldene. The yellow, green, gray, blue, violet, and red colors represent Au, B, Al, N, P and S atoms, respectively. All structures retain their flat nature after doping with the various elements.

View Article Online
DOI: 10.1039/D4CP03087G

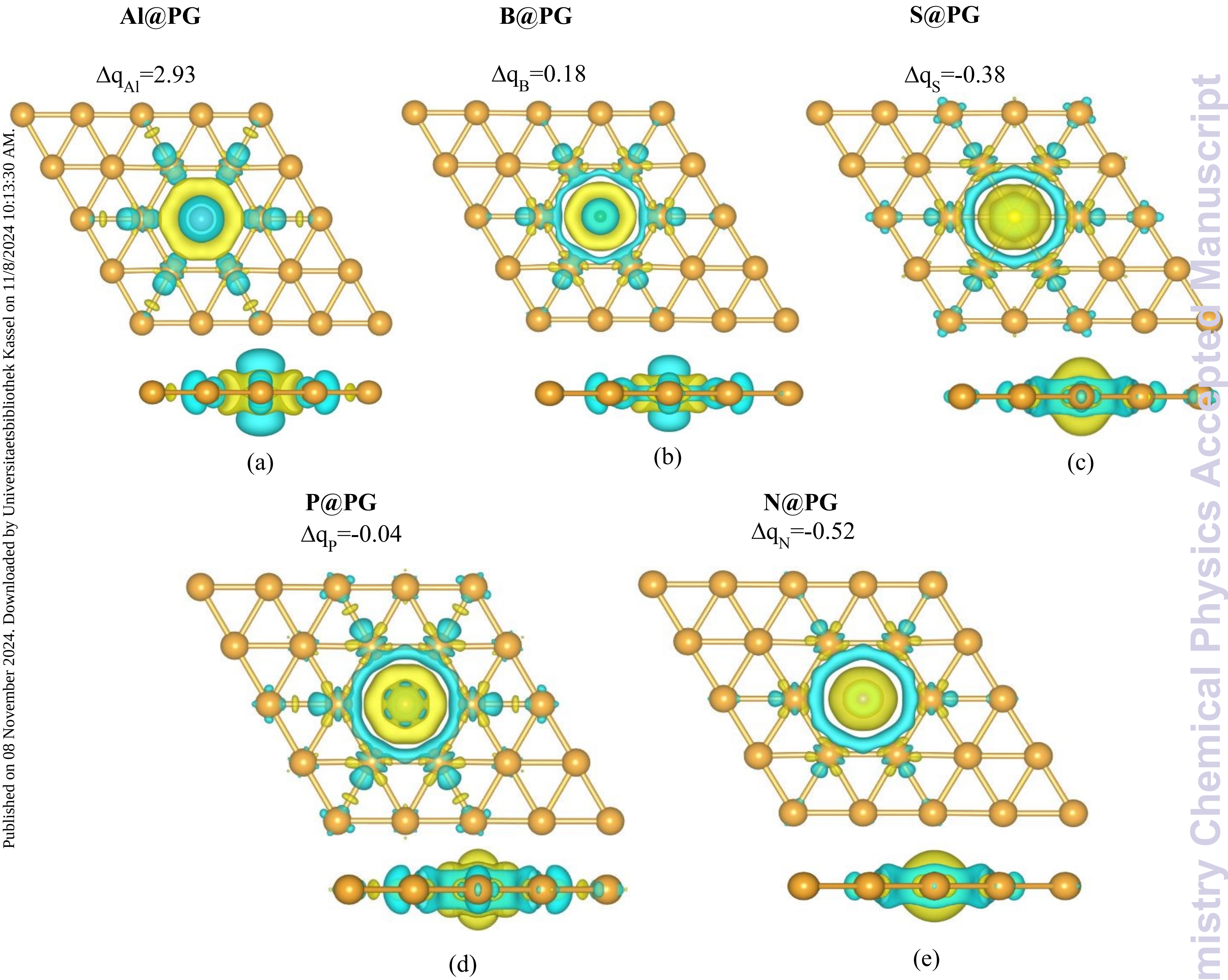

Figure 5 Top and side view of charge density differences in (a) Al@PG, (b) B@PG, (c) S@PG, (d) P@PG, and (e) N@PG systems. Al and B atoms act as electron donors, while S, P and N atoms act as electron acceptors. (Yellow indicates charge depletion, whereas blue indicates charge accumulation)

3.4 CO_2 adsorption on pristine goldene (CO_2@PG)

View Article Online
DOI: 10.1039/D4CP03087G

To investigate the activation of CO_2 at goldene, we have explored different adsorption sites on the goldene sheet, i.e. on top the Au atom (A-site), at a bridge (B-site), and in the centre of a triangular Au ring (C-site), as shown in **Figure 1(a)**. We have also tried different initial orientations (both vertical and horizontal) of the CO_2 molecules over the goldene sheet. The most stable configuration of CO_2 after adsorption is shown in **Figure 6,** while all other configurations are presented in **Figures S3** and **S4** of the SI. We found that the most stable CO_2 configuration on the pristine goldene sheet is the one where we initially placed the CO_2 molecule over the A site in a vertical orientation, which led to physisorption of the CO_2 molecule with an adsorption energy of -24.0 kJ/mol energy on a 4×4×1 supercell. We repeated our calculations over 5×5×1 and 6×6×1 supercells and found E_{ads} to be -24.6 and -24.8 kJ/mol, i.e. showing negligible variation. Hence, we have carried out all other calculations on a 5×5×1 supercell. Since the CO_2 molecule remains almost linear upon adsorption, the interaction between PG and CO_2 molecules can be considered physisorption due to strong Van der Waals interactions (**Figure 6**). After adsorption, the bond length of the CO_2 molecule (C-O) was 1.18 Å, and the CO_2 molecule acts as an electron acceptor, gaining an electronic charge of -0.02 e^- (**Table 4)**. Due to the weak interaction between PG and CO_2 molecules, the distribution of energy states in PDOS (**Figure 7**) and EBS (**Figure S5**) remains the same.

3.5 CO_2 adsorption on partially vacant goldene (CO_2@MG, CO_2@DG and CO_2@TG)

Next, we investigated the interaction of CO_2 molecules over different vacancy-containing goldene sheets, i.e. mono- (MG), di- (DG) and tri-vacancy (TG) goldene sheets, by placing CO_2 molecules over the sheets in different initial configurations and orientations. These configurations include one O atom of CO_2 facing Au and another lying above vacancies, a C atom of CO_2 lying above an Au atom of goldene (near a vacancy), and an O atom placed near vacancy sites (**Figure S6, S7 and S8)**. The calculated adsorption energies (E_{ad_def}), adsorption height and bond lengths of all of these considered configurations are listed in **Table S2** of the SI.

The most stable configurations of CO_2 adsorbed on each partially vacant nanosheet are tabulated in **Table 4.** CO_2 interacts with MG (configuration MG-1), DG (configuration DG-2), and TG (configuration TG-3) with adsorption energies of -25.6 kJ/mol, -25.1 kJ/mol and -31.0 kJ/mol, respectively. Note that the adsorption energies of CO_2 on PG, MG, and DG are almost the same, and only on TG it increases slightly, by about ~6 kJ/mol. The adsorption heights of the adsorbate

View Article Online
DOI: 10.1039/D4CP03087G

above the surface MG, DG, and TG are 2.94 Å, 2.55 Å, and 2.03 Å, respectively. In all cases, the CO_2 molecule remains almost linear; thus, similar to CO_2@PG, the adsorption of CO_2 on vacancy-containing goldenes can be categorized as physisorption. We have also investigated adsorption at different tri-vacancy defects as discussed in the earlier section, i.e. angle, line and triangle. The adsorption energy of CO_2 converges to the same value (-22.73 kJ/mol) for the line and angle tri-vacancy structures, but at the triangle tri-vacancy it reaches -31.0 kJ/mol. The most stable configurations of CO_2 on MG, DG, and TG are shown in **Figure 6**. All other configurations at different adsorption sites, along with their adsorption energies and adsorption heights, are provided in **Figures S6, S7, and S8**.

In all three cases, the weak physisorption of CO_2 can be explained through the PDOS, where no contribution of O and C atoms of the CO_2 is found near the Fermi level (**Figure 7)**. Also, the overlapping energy levels of energy states do not disappear, so the systems remain metallic. Additionally, we have also verified our choice of the 5×5×1 supercell for the CO_2 adsorption calculations by repeating the calculations in a 6×6×1 supercell, where we noted only nominal changes in the CO_2 molecule adsorption energies, i.e. -26.19 kJ/mol and -29.73 kJ/mol for the DG and TG systems, respectively, in the 6×6×1 supercell.

We found that vacancies can promote CO_2 activation where tri-vacancy-containing structures lead to a CO_2 adsorption energy, which is 25.6% higher than on the pristine goldene sheets. The presence of vacancies promotes charge transfer between the CO_2 molecules and goldene sheets, as vacancy sites act as electron donors facilitating a better interaction with molecules.

3.6 CO_2 adsorption on X-doped goldene (CO_2+X@PG)

To explore the effect of adding X (= Al, B, S, N, P) dopants in PG on CO_2 adsorption, various alignments of CO_2 molecules near the X atom were investigated (see **Figures S9-S13**), as summarized in **Table S3** of SI. The adsorption energy (E_{ad_Al}) of the CO_2 molecule on the Al@PG system (see Al-2 configuration of **Figure S9**) is found to be -38.0 kJ/mol with an adsorption height of 2.66 Å, which is 1.54 times greater than its value on PG (**Figure 6**). As the CO_2 molecule remains almost linear after adsorption on Al@PG, this can also be considered physisorption. Before interaction with CO_2, the net charge on the Al atom was $2.93e^-$ which remained the same. After interaction with this doped goldene sheet, the CO_2 molecule accumulates -0.02 e^- charge

View Article Online
DOI: 10.1039/D4CP03087G

(**Table S4)**. Thus, doping the goldene with Al does not contribute to charge transfer and improved interaction between CO_2 and goldene nanosheet.

In contrast, the adsorption energy of the CO_2 molecule is altered significantly by its adsorption on the B@PG (**Figure 6(f)**) system (B-2 initial configuration of **Figure S10**). Here, we note molecular deformation to a bond angle of 119.9° and an increment in C-O bond length up to 1.35 Å, revealing strong chemisorption and activation of CO_2 on the B@PG sheet. A comparison with the literature shows that the adsorption energy of CO_2 on B@PG (E_{ad_B} =-138.9 kJ/mol) is more than that on B-doped germanene, (-48.24 kJ/mol) [57], indicating that B@PG is a better candidate than B@Ge for CO_2 activation. Doping by the B atom in goldene reduces the CO_2 molecule as the B atom donates 1.37e^- electrons, and the CO_2 molecule gains -1.22e^- in charge (**Figure 8)**. This net negative charge on the CO_2 molecule suggests the initiation of the reduction process in a potential chain of further reduction reactions towards fuels and chemical products.

The adsorption of the CO_2 molecule on S@PG (**Figure 6(g)**) and P@PG (**Figure 6(h)**) leads to lower adsorption energies with E_{ad_S}=-26.78 kJ/mol (S-1 initial configuration of **Figure S11**) and E_{ad_P}=-37.67 kJ/mol (P-1 initial configuration of **Figure S12**), respectively, due to the relative inactivity of S@PG and P@PG.

In the case of the N-doped goldene sheet (N@PG), we observe strong chemisorption with a calculated adsorption energy E_{ad_N} = -163.7 kJ/mol (N-1 initial configuration of **Figure S13**), as shown in Figure 6(i)**.** Here, we note considerable changes in the geometry of the CO_2 molecule, which bends to 120.9° and the C-O bond elongates to 1.28 Å. Also, the CO_2 molecule loses 0.66e^- of charge due to activation on N@PG **Figure 6(i)**). A comparison with an earlier computational work on CO_2 adsorption on the N-doped germanium 2D sheet reveals that the N@PG sheet is better suited for CO_2 activation, as the calculated CO_2 adsorption energy on the germanium sheet was only -92.6 kJ/mol[57]. As such, we only observed strong chemisorption and activation of CO_2 molecules onto the B- and N-doped goldene sheets.

We next studied the PDOS and EBS due to CO_2 interaction with various doped goldene sheets. For PG, the sharpest peak arises near the -2 eV to -3eV energy range and it remains at almost the same position even after vacancy formation, doping, and CO_2 activation. This consistency means that despite many modifications in atomic arrangements, the electronic properties of goldene (such as electrical conductivity and metallic nature) are preserved within the energy interval -2eV to -

View Article Online
DOI: 10.1039/D4CP03087G

3eV. Although the changes generate novel small and sharp peaks (after doping with Al, B and P), no separation is found between the energy bands. The closely packed energy levels in the EBS (**Figure S5**) confirm this trend of electronic characteristics of goldene.

Table 4 Adsorption energy E_{ads} (kJ/mol), adsorption height h (Å), bond lengths l (Å), bond angle θ (°), buckling height δ (Å) and charge transfer Δq_{co2} of pristine, vacancy-containing and doped goldene for the most stable configurations of CO_2 after adsorption

System	E_{ads}	h	l			θ	δ	Δq_{co2}
			Au-Au	C-O	Au-X			
CO_2@PG	-24.6	3.15	2.74	1.18	---	179.9°	0.07	-0.02
CO_2@MG	-25.6	2.94	2.76	1.17	---	179.8°	0.06	-0.04
CO_2@DG	-25.1	2.55	2.77	1.18	---	179.8°	0.10	-0.05
CO_2@TG	-30.9	2.03	2.76	1.18	---	179.7°	0.07	-0.05
CO_2+Al@PG	-38.0	2.66	2.76	1.19	2.69	178.6°	0.17	-0.09
CO_2+B@PG	-138.9	1.17	2.92	1.39	3.35	119.9°	0.82	-1.22
CO_2+S@PG	-26.8	3.40	2.75	1.17	2.99	179.0°	0.31	-0.03
CO_2+P@PG	-37.7	3.38	2.75	1.17	2.90	179.9°	0.66	-0.02
CO_2+N@PG	-163.7	1.20	2.90	1.28	3.59	120.9°	0.84	0.66

In summary, neither n-type (N and P) nor p-type (B and Al) doping can generate a band gap in goldene. The charge transfer between all considered systems of goldene and the CO_2 molecule is shown in **Figure 8.** After interaction of the CO_2 molecule with the PG, DG and X@PG systems, the contribution of the d-orbital of the Au atom remains almost the same, as well as dominating in the VB. Thus, the d-orbital of the Au atom does not participate in hybridization with the atomic orbitals of the CO_2 molecule and it is not involved in bonding with CO_2. The interaction arises through the s and p orbitals of Au and the p-orbital of the O atom of CO_2 as small peaks of O(p) orbital appear near -4 eV, which indicates a selective orbital interaction between CO_2 and the various goldene systems.

We have summarized the optimized parameters and adsorption characteristics of the most stable configurations of CO_2 molecules after adsorption for all considered systems in **Table 4**. The gold

View Article Online
DOI: 10.1039/D4CP03087G

5d and 6s orbitals interact with the 2p orbitals of B and N. The B 2p orbitals can overlap with the Au d-orbitals, leading to some covalent character in the bond and a favorable bonding interaction. The overlap is even stronger for N owing to its higher electronegativity, causing an enhanced charge transfer. N can also form strong bonds by drawing electron density from Au.

Although Al shows strong binding to the goldene sheet, its large atomic size, low electronegativity, and poor orbital overlap with CO_2 result in primarily physical interactions, leading to physisorption with minimal charge transfer (-0.09 e^-). In contrast, B and N enable strong chemisorption of CO_2 owing to better charge redistribution and orbital compatibility with both Au and CO_2. B, with its moderate electronegativity and smaller size, loses a small amount of charge (+0.18) but facilitates significant charge transfer (-1.22 e^-) upon CO_2 adsorption, indicating strong bonding. N, with its high electronegativity and ability to attract electrons (-0.52) from Au, exhibits a strong interaction, with a charge transfer of 0.66 to CO_2. In contrast, P (-3.88 eV) and S (-4.52 eV) demonstrate weaker binding energies to the goldene sheet, which correlates with their limited charge transfer capabilities upon CO_2 adsorption. Both P and S have similar or slightly lower electronegativities compared to Au, leading to poor charge redistribution and weak interactions with CO_2. Their larger atomic sizes and ineffective orbital overlap with CO_2 contribute to the lack of significant charge transfer during adsorption, resulting in physisorption rather than chemisorption. The introduction of Au vacancies in the goldene sheet caused a nominal increase in CO_2 adsorption energies by providing more suitable interaction sites. Our findings provide valuable insights into CO_2 activation mechanisms and underscore the potential of goldene for electrochemical CO_2 conversion applications.

We would like to emphasize that the present work employs calculations based on the GGA and PBE methods which are widely accepted approaches to describe the electronic properties and catalytic characteristics of 2D materials. Moreover, although we understand that the choice of functionals may affect the absolute values of the calculated adsorption energies, the observed trends of interaction strength and the nature of adsorption will remain unchanged.

View Article Online
DOI: 10.1039/D4CP03087G

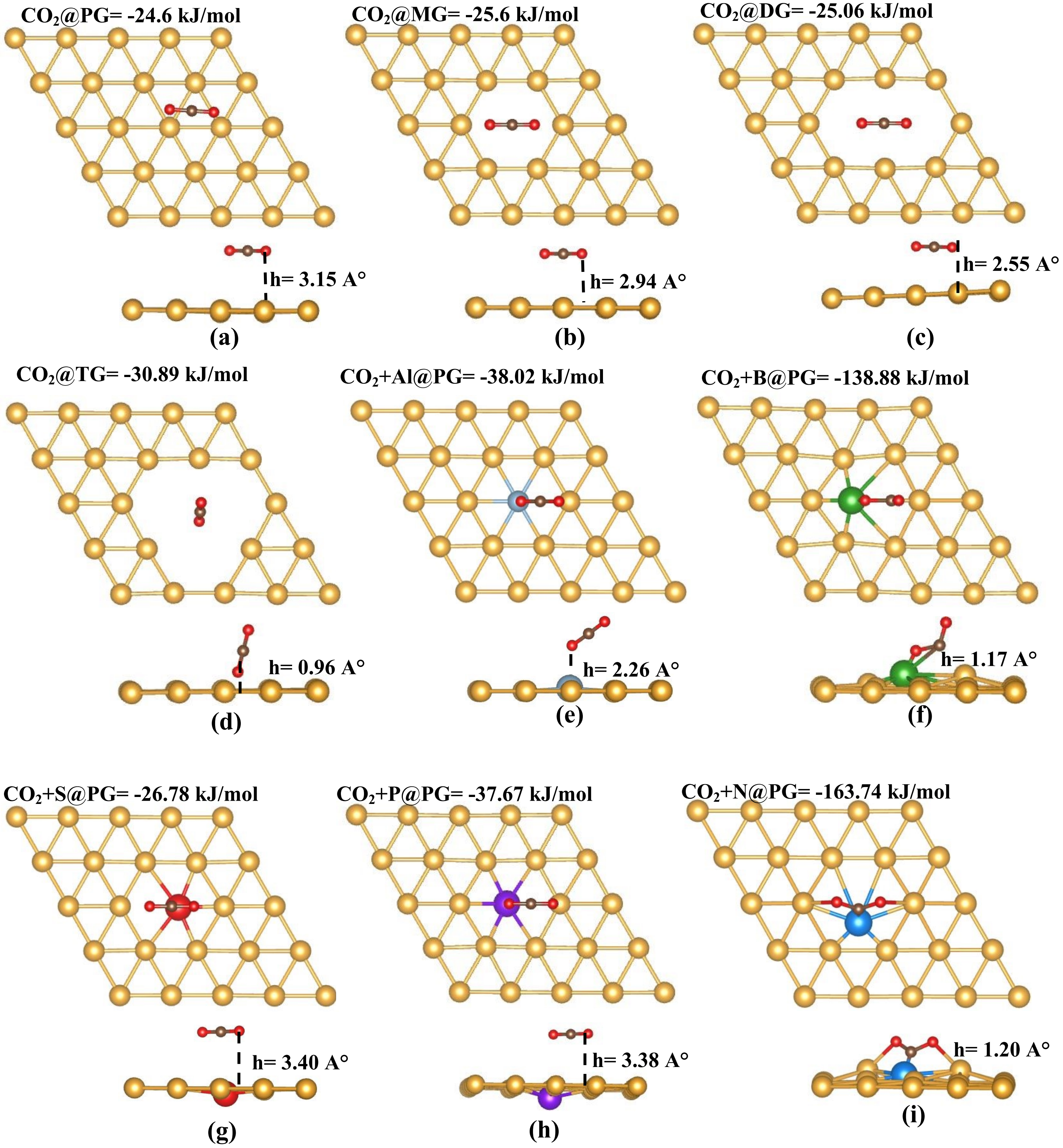

Figure 6 Top and side view of most stable configurations of (a) CO_2@PG (b) CO_2@MG (c) CO_2@DG (d) CO_2@TG (e)CO_2+Al@PG (f) CO_2+B@PG (g) CO_2+S@PG (h) CO_2+P@PG (i) CO_2+N@PG systems. CO_2 adsorbs chemically at B@PG and N@PG systems.

View Article Online
DOI: 10.1039/D4CP03087G

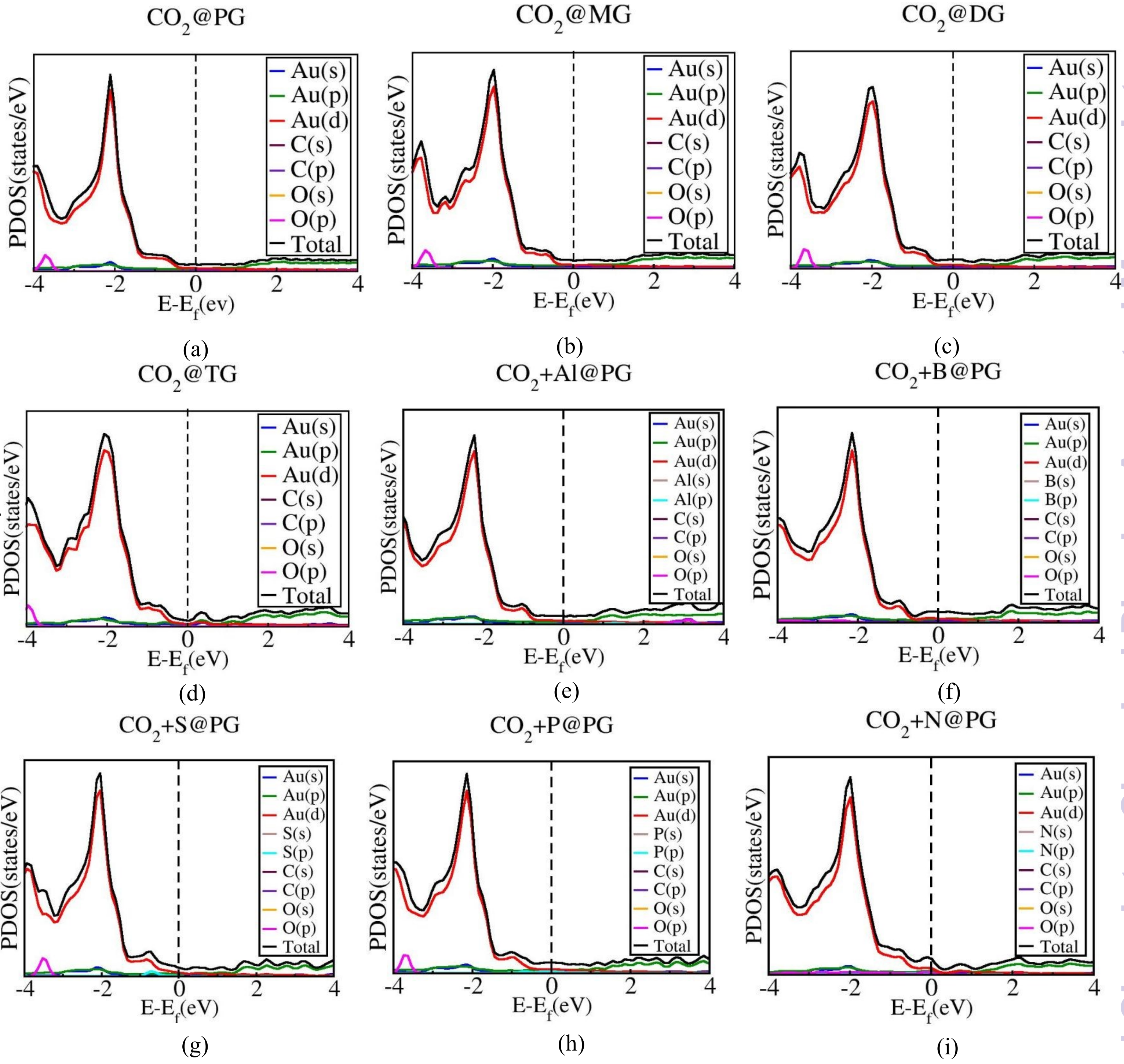

Figure 7 PDOS of most stable configurations of CO_2 on (a)PG (b) MG (c) DG (d) TG (e) Al@PG (f) B@PG (g) S@PG (h) P@PG and (i) N@PG systems. The Fermi Level is set at zero and is represented by a dotted line. After CO_2 adsorption, goldene remains metallic.

View Article Online
DOI: 10.1039/D4CP03087G

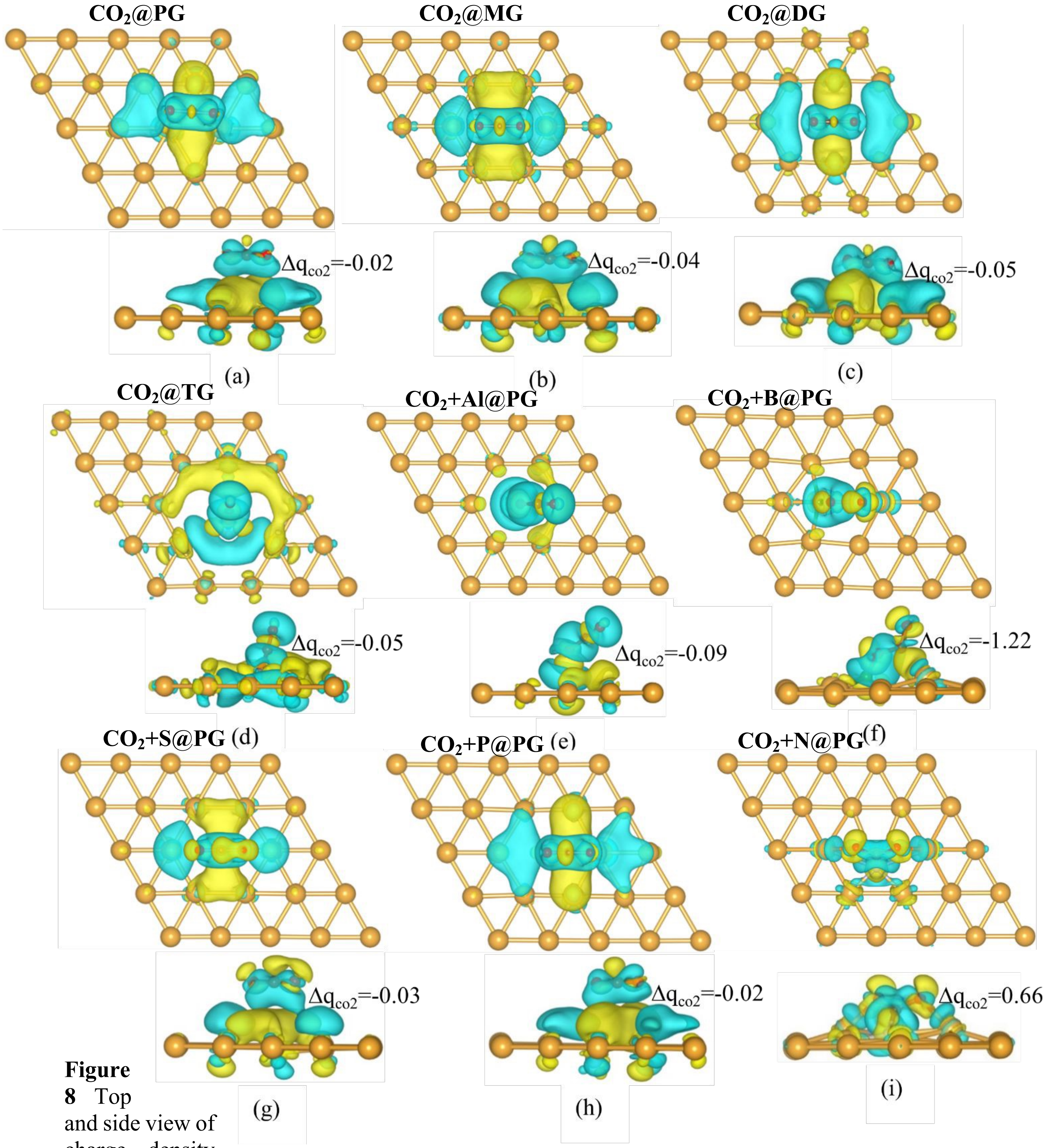

Figure 8 Top and side view of charge density difference after CO_2 adsorption on (a)PG (b) MG (c) DG (d) TG (e) Al@PG (f) B@PG (g) S@PG (h) P@PG (i) N@PG systems. Maximum charge transfer at B and N doped occurs between CO_2

View Article Online
DOI: 10.1039/D4CP03087G

and B@PG system. (Yellow indicates charge depletion, whereas blue indicates charge accumulation)

4 Conclusion

In this work we have employed DFT-based simulations to investigate CO_2 adsorption and activation on pristine, partially vacant, and doped 2D goldene sheets. We first explored the interaction of the CO_2 molecule with PG, which exhibited weak physisorption with an adsorption energy of -24.6 kJ/mol. We next engineered defects in goldene sheets by introducing vacancies, where we investigated single, double, and tri-vacancy systems. From our calculated values of the defect formation energies, we can conclude that goldene is susceptible to vacancy formations. The presence of vacancies slightly enhances the interaction of CO_2 with the goldene sheet, with calculated adsorption energies of -25.6 kJ/mol, -25.1 kJ/mol, and -31.0 kJ/mol for MG, DG, and TG, respectively. After the vacancy creation and interaction with the CO_2 molecule, goldene remains metallic. We have further explored the effects of adding different dopants (Al, B, S, N, P) on the CO_2 activation characteristics of goldene sheets and found that B and N doping activates CO_2 on the goldene sheets. Our computational investigations of pristine, vacancy-containing, and doped goldene sheets highlights the significant differences in CO_2 activation mechanisms that can be obtained when the goldene sheets are adapted through vacancy formation or doping.

Supplementary Information

We have provided all investigated configurations of CO_2 molecules on the pristine, vacancy-containing and doped goldene nanosheets in the supplementary information (SI). **Figure S1** represents mono-, di-, and tri-vacancies in the 4×4×1 and 6×6×1 supercells of goldene. The EBS of defective and doped goldene is shown in **Figure S2**. **Figures S3** and **S4** show CO_2 adsorption on the 4×4×1 and 5×5×1 supercells of pristine goldene, respectively. **Figure S5** represents the EBS after the adsorption of CO_2 at different goldene systems. **Figures S6**, **S7** and **S8** represent CO_2 adsorption at mono-, di-, and tri-vacancy goldene sheets. Figures **S9, S10**, **S11**, **S12** and **S13** show CO_2 activation on Al, B, S, P, and N-doped goldene sheets, respectively. The adsorption energies, heights, bond lengths and bond angles of the CO_2 molecule after adsorption on the

View Article Online
DOI: 10.1039/D4CP03087G

pristine, vacancy-containing and doped goldene are summarized in **Tables S1**, **S2**, and **S3,** respectively. **Table S4** contains the Bader charge transfer for dopants and CO_2 molecules.

Acknowledgements

A.K.M. acknowledges the SERB SURE grant (SUR/2022/004935-year 2023) and SEED 2021 grant from UPES for computational facilities. Via our membership of the UK's HEC Materials Chemistry Consortium, which is funded by EPSRC (EP/X035859), we also acknowledge the use of the ARCHER2 UK National Supercomputing Service (https://www.archer2.ac.uk).

References

1 L. M. Yang, M. Dornfeld, T. Frauenheim and E. Ganz, *Physical Chemistry Chemical Physics*, 2015, **17**, 26036–26042.

2 X. Wang, C. Wang, C. Chen, H. Duan and K. Du, *Nano Letters*, 2019, **19**, 4560–4566.

3 S. K. Sharma, R. Pasricha, J. Weston, T. Blanton and R. Jagannathan, *ACS Applied Materials & Interfaces*, 2022, **14**, 54992–55003.

4 S. Kashiwaya, Y. Shi, J. Lu, D. Sangiovanni, M. Andersson, J. Rosen and L. Hultman, 2023, DOI:10.21203/rs.3.rs-2807259/v2.

5 M. Sekulla, M. Kohns and M. Richter, *Industrial and Engineering Chemistry Research*, 2023, **62**, 19884–19892.

6 R. Grisel, K.-J. Weststrate, A. Gluhoi and B. E. Nieuwenhuys, *Gold Bulletin*, 2002, **35**, 39-45.

7 M. López-Haro, J. J. Delgado, J. M. Cies, E. Del Rio, S. Bernal, R. Burch, M. A. Cauqui, S. Trasobares, J. A. Pérez-Omil, P. Bayle-Guillemaud and J. J. Calvino, *Angewandte Chemie - International Edition*, 2010, **49**, 1981–1985.

8 H. Grönbeck, A. Curioni and W. Andreoni, *Journal of American Chemical Society*, 2000, **122**, 3839–3842.

9 N. D. S. Canning, D. Outka and R. J. Madix, *Surface Science, 1984,* **141**, 240-254.

10 R. Liu, *Computational and Theoretical Chemistry*, 2013, **1019**, 141–145.

11 Y. Huang, E. Sutter, N. N. Shi, J. Zheng, T. Yang, D. Englund, H. J. Gao and P. Sutter, *ACS Nano*, 2015, **9**, 10612–10620.

12 J. N. Coleman, *Accounts of Chemical Research,* 2013, **46**, 14-22.

View Article Online
DOI: 10.1039/D4CP03087G

13 Z. Li, N. H. Attanayake, J. L. Blackburn and E. M. Miller, *Energy & Environmental Science,* 2021, **14**, 6242-6286.

14 X. Ling, W. Fang, Y. H. Lee, P. T. Araujo, X. Zhang, J. F. Rodriguez-Nieva, Y. Lin, J. Zhang, J. Kong and M. S. Dresselhaus, *Nano Letters*, 2014, **14**, 3033–3040.

15 T. Zhang, H. Sun, F. Wang, W. Zhang, J. Ma, S. Tang, H. Gong and J. Zhang, *Theoretical Chemistry Accounts*, **136**, 1-8.

16 Y. Zhao, M. Zheng, J. Wu, X. Guan, A. Suwardi, Y. Li, M. Lal, G. Xie, G. Zhang, L. Zhang and J. T. L. Thong, *Nanoscale*, 2021, **13**, 11561–11567.

17 U. J. Etim, C. Zhang and Z. Zhong, *Nanomaterials*, 2021, **11**, 3265.

18 A. Junkaew and R. Arróyave, *Physical Chemistry Chemical Physics*, 2018, **20**, 6073–6082.

19 H. Li, M. Huang and G. Cao, *Physical Chemistry Chemical Physics*, 2016, **18**, 15110–15117.

20 J. Dai, J. Yuan and P. Giannozzi, *Applied Physics Letters*, 2009, **95**.

21 M. P. K. Sahoo, J. Wang, Y. Zhang, T. Shimada and T. Kitamura, *Journal of Physical Chemistry C*, 2016, **120**, 14113–14121.

22 M. Manzoor, K. Kumar, A. K. Mishra, B. A. Al-Asbahi and R. Sharma, *Solid State Communications*, 2024, **386,** 115527**.**

23 D. Maarisetty, R. Mary, D. R. Hang, P. Mohapatra and S. S. Baral, *Journal of CO2 Utilization*, 2022, **64,** 102175.

24 K. Akhtar, S. Sarfaraz and K. Ayub, *Materials Science in Semiconductor Process*, 2024, **184**, 108784

25 C. Wang, Y. Fang, H. Duan, G. Liang, W. Li, D. Chen and M. Long, *Solid State Communications*, 2021, **337**, 114436.

26 T. Hussain, T. Kaewmaraya, S. Chakraborty and R. Ahuja, *Journal of Physical Chemistry C*, 2016, **120**, 25256–25262.

27 H. Lee, K. Paeng and I. S. Kim, *Synthetic Metals*, 2018**, 244,** 36–47.

28 R. Lv and M. Terrones, *Materials Letters*, 2012, **78**, 209–218.

29 C. Vogt, M. Monai, E. B. Sterk, J. Palle, A. E. M. Melcherts, B. Zijlstra, E. Groeneveld, P. H. Berben, J. M. Boereboom, E. J. M. Hensen, F. Meirer, I. A. W. Filot and B. M. Weckhuysen, *Nature Communications*, 2019, **10**, 5330.

30 Z. Suo, J. Dai, S. Gao and H. Gao, *Results and Physics,* 2020, **17**, 103058.

View Article Online
DOI: 10.1039/D4CP03087G

31 S. S. Varghese, S. Swaminathan, K. K. Singh and V. Mittal, *Computational Condensed Matter*, 2016, **9**, 40–55.

32 Q. Feng, J. Liu, Y. Yang, D. Pan, Y. Xing, X. Shi, X. Xia and H. Liang, *Journal of Alloys Compounds*, 2016, **687**, 964–968.

33 M. Shafiei, F. Hoshyargar, J. Lipton-Duffin, C. Piloto, N. Motta and A. P. OMullane, *Journal of Physical Chemistry C*, 2015, **119**, 22208–22216.

34 B. Hoex, J. Schmidt, R. Bock, P. P. Altermatt, M. C. M. Van De Sanden and W. M. M. Kessels, *Applied Physics Letters*, 2007, **91**, 112107.

35 M. Tsuji, T. Imajo, N. Saitoh, N. Yoshizawa, T. Suemasu and K. Toko, *Journal of Physics D: Applied Physics*, 2019, **53**, 075105.

36 A. Shokuhi Rad and V. Pouralijan Foukolaei, *Synthetic Metal*, 2015, **210**, 171–178.

37 M. M. Monshi, S. M. Aghaei and I. Calizo, *Surface Science*, 2017, **665**, 96–102.

38 Z. Zheng and H. Wang, *Chemical Physics Letters*, 2019, **721**, 33–37.

39 J. M. Zhang, W. T. Song, K. W. Xu and V. Ji, *Computational Material Science*, 2014, **95**, 429–434.

40 X. Zhang, D. Zhang, F. Xie, X. Zheng, H. Wang and M. Long, *Physics Letters, Section A: General, Atomic and Solid-State Physics*, 2017, **381**, 2097–2102.

41 R. Ma, K. Wang, C. Li, C. Wang, A. Habibi-Yangjeh and G. Shan, *Nanoscale Advances*, 2022, **4**, 4197–4209.

42 X. Zhan, X. Tong, M. Gu, J. Tian, Z. Gao, L. Ma, Y. Xie, Z. Chen, H. Ranganathan, G. Zhang and S. Sun, *Nanomaterials*, 2022, **12,** 1141.

43 H. Seema, K. C. Kemp, N. H. Le, S. W. Park, V. Chandra, J. W. Lee and K. S. Kim, *Carbon N Y*, 2014, **66**, 320–326.

44 A. K. Mishra and S. Mishra, *Journal of Molecular Graphics and Modeling*, 2019, **93**, 107446**.**

45 N. Kumar, K. S. Subrahmanyam, P. Chaturbedy, K. Raidongia, A. Govindaraj, K. P. S. S. Hembram, A. K. Mishra, U. V. Waghmare and C. N. R. Rao, *ChemSusChem*, 2011, **4**, 1662–1670.

46 A. Gutiérrez, S. Rozas, P. Hernando, R. Alcalde, M. Atilhan and S. Aparicio, *Journal of Molecular Liquids*, 2022, **336**, 120285.

47 P. Giannozzi, S. Baroni, N. Bonini, M. Calandra, R. Car, C. Cavazzoni, D. Ceresoli, G. L. Chiarotti, m. Cococcioni, I. Dabo, A. D. Corso, S. Fabris, G. Fratesi, S. de Gironcoli, R. Gebauer, U. Gerstmann, C. Gougoussis, A. Kokalj, M. Lazzeri, L. Martin-Samos, N. Marzari, F. Mauri, R. Mazzarello, S. Paolini, A. Pasquarello, L. Paulatto, C. Sbraccia, S.

View Article Online
DOI: 10.1039/D4CP03087G

Scandolo, G. Sclauzero, A. P. Seitsonen, A. Smogunov, P. Umari and R. M. Wentzcovitch, *Journal of Physics: Condensed Matter,* 2009, **21**, 395502.

48 J. P. Perdew, K. Burke and M. Ernzerhof, *Physical Reviews Letters,*1996, **18**, 3865.

49 G. K. H. Madsen, *Physical Reviews B-Condensed Matter and Material physics,* 2007, **19**, 195108.

50 P. Haas, F. Tran, P. Blaha, K. Schwarz and R. Laskowski, *Physical Review B- Condensed Matter and Material Physics*, 2009, **19**, 195109.

51 S. Grimme and M. Steinmetz, *Physical Chemistry Chemical Physics*, 2013, **15**, 16031–16042.

52 N. A. W. Holzwarth, A. R. Tackett and G. E. Matthews, Computer Physics Communications, 2001, **135**, 329-347.

53 C. Li, S. Yang, S. S. Li, J. B. Xia and J. *Journal of Physical Chemistry C*, 2013, **117**, 483–488.

54 G. Yang, L. Li, W. B. Lee and M. C. Ng, *Science and Technology of Advanced Materials*, 2018, **19**, 613–648.

55 H. Hernández Cocoletzi and J. E. Castellanos Águila, *Superlattices Microstructure*, 2018, **114**, 242–250.

56 A. K. Shiraz, A. Y. Goharrizi and S. M. Hamidi, *Materials Research Express*, 2019, **10**, 1050c2.57

View Article Online
DOI: 10.1039/D4CP03087G

Data availability Statements: The data supporting this article have been included as part of the Supplementary Information.